Effects of initial conditions on a wavelet-decomposed turbulent near-wake

Akira Rinoshika*
Department of Mechanical Systems Engineering, Yamagata University, 4-3-16 Jonan, Yonezawa-shi, Yamagata 992-8510, Japan

Yu Zhou†
Department of Mechanical Engineering, The Hong Kong Polytechnic University, Hung Hom, Kowloon, Hong Kong, China
(Received 7 January 2005; revised manuscript received 2 February 2005; published 12 April 2005)

The effect of initial conditions on the turbulent structures of various scales in a near-wake has been investigated for two wake generators, i.e., a circular cylinder and screen of 50% solidity, of the same characteristic dimension. Velocity data were obtained at x/h (x and h are the streamwise distance downstream and the height of the wake generators, respectively) =20 using 16 X wires, eight aligned in the plane of mean shear and eight in the plane parallel to both the cylinder axis and the flow direction. A wavelet multiresolution technique was used to decompose the velocity data into a number of wavelet components based on the central frequencies, which correspond to the scales of turbulent structures. It was found that the behaviors of intermediate- as well as large-scale structures depend on the initial conditions. In the circular cylinder wake, the large- and intermediate-scale structures make the largest (and comparable) contribution to Reynolds stresses, but in the screen wake there is a significant difference in the contribution between the two types of structures. The two-dimensionality of the wavelet component is also examined.

DOI: 10.1103/PhysRevE.71.046303 PACS number(s): 47.27.Vf, 47.32.Cc, 07.05.Kf

I. INTRODUCTION

The topology and transport characteristics of the turbulent structure in the wake that depend on the wake-generating bodies or initial conditions have been well-established. Sreenivasan [1] found that different wake-generating bodies produced substantial differences in the manner wakes, even if the mean velocity profile exhibited the same shape. Wygnanski *et al.* [2] examined a dependence of the normalized distributions of the longitudinal turbulence intensity on the initial conditions. Although the different vortical behavior in the wake as the initial conditions differ was confirmed by Louchez *et al.* [3] and Matsumura *et al.* [4], this difference has not been well documented. The turbulent near-wake vortices behind various wake-generating bodies were studied in detail by Zhou and Antonia [5]. They observed a significant variation in the flow structure and momentum transport characteristics of turbulent vortices. However, due to the limitation of their detection scheme, they could not provide any information on the relationship between initial conditions and organized structures other than the large-scale ones. In the past decade, there has been a growing interest in the use of wavelet analysis for extracting new information on the turbulence structures of various scales [6–11]. Recently, Rinoshika and Zhou [12] developed an orthogonal wavelet multiresolution technique to analyze the turbulent near-wake of a circular cylinder. Using this technique, the flow is decomposed into a number of wavelet components based on their characteristic or central frequencies, which are representative of the turbulent structures of different scales. The objective of this work is to study the dependence of the turbulent structures of various scales on initial conditions. The same orthogonal wavelet multiresolution technique as developed by Rinoshika and Zhou [12] was used presently.

Measurements were conducted in the near-wake generated by a circular cylinder and a screen of 50% solidity, respectively. The velocity data were obtained using a number of X wires. The details are given in Sec. II. Section III introduces the wavelet decomposition technique briefly. Section IV presents sectional streamlines of the wavelet components. The contributions the wavelet components make to the time-averaged Reynolds stresses and velocity correlations are estimated and compared between the two wake generators in Sec. V. The work is concluded in Sec. VI.

II. EXPERIMENTAL DETAILS

Experiments were conducted in an open-return low-turbulence wind tunnel with a 2.4-m-long working section (0.35 m $\times$ 0.35 m) in Professor R. A. Antonia's laboratory at The University of Newcastle. The bottom wall was tilted to achieve a zero streamwise pressure gradient. The experimental arrangement can be found in Zhou and Antonia [5]. A circular cylinder and a screen of 50% solidity with the same height (h=12.5 mm) were used to generate the wake, respectively; each was installed in the midplane and spanned the full width of the working section, 0.20 m from the exit plane of the contraction. This resulted in a blockage of about 3.6%. The streamwise length of the screen is about 0.5 mm. Measurements were made at x/h=20 (x is the streamwise distance downstream of the cylinder) and a constant free stream velocity (U_∞=6.7 m/s). The corresponding Reynolds number Re_h ($\equiv U_\infty h/\nu$) was 5600. The Kolmogorov length scale was estimated to be about 0.16 mm. Table I summarizes the characteristic flow parameters for the two wake generators,

*Corresponding author, also known as Hui LI. Email address: rinosika@yz.yamagata-u.ac.jp; FAX: +81-238-26-3225.
†Email address: mmyzhou@polyu.edu.hk

TABLE I. Characteristic wake parameters.

Wake generator	h (mm)	θ (mm)	Re_h	Re_θ	L (mm)	U_1/U_∞ (%)	x/h	x/θ
Cylinder	12.5	5.9	5600	2600	14	0.2	20	42
Screen	12.5	4.1	5600	1800	10	0.33	20	61

where Re_θ is the Reynolds number based on the momentum thickness θ, L is the mean velocity half-width, and U_1 is the centerline velocity defect.

Two orthogonal arrays, each consisting of eight X wires, were used. One was aligned in the (x,y) plane, i.e., the plane of mean shear, and the other in the (x,z) plane, which was parallel to both the cylinder axis and the streamwise direction. The 16 X wires of the two arrays allow velocity fluctuations u and v in the (x,y) plane and u and w in the (x,z) plane to be obtained simultaneously. The nominal spacing between X wires in both planes was about 5 mm except for a relatively large gap (=9.1 mm) between the fourth and fifth X wires in the (x,z) plane. While the probe rake in the (x,y) plane was fixed, the other in the (x,z) plane was movable so that data could be obtained at different (x,z) planes. Since only one set of data obtained in the (x,y) plane was presently analyzed, both probe rakes may be considered fixed. The physical blockage caused by these arrays, cables, and supports was estimated to be about 3%. Several types of measurements [13] indicated that the interference to the flow due to the two arrays was negligible.

Wollaston (Pt-10% Rh) wires, 5 μm in diameter and about 1 mm in working length, were operated with constant temperature circuits. Signals from the circuits were offset, amplified, and then digitized using two 16-channel (12-bit) A/D (analog-to-digital) boards and two personal computers at a sampling frequency of $f_s=3.5$ kHz per channel (the cutoff frequency was 1600 Hz). Data acquisition by the two computers was synchronized using a common external trigger pulse. The wires were calibrated for velocity and yaw, and continuously checked for drift. There was no appreciable drift observed since sampling of each set of data was about 38 s and the total duration for the acquisition of a number of sets of data was completed in a few minutes. The sampled data were processed based on velocity and yaw calibrations to obtain signals proportional to u, v, and w, together with the local mean velocities $\overline{U}$, $\overline{V}(\approx 0)$, and $\overline{W}(\approx 0)$.

III. ORTHOGONAL WAVELET DECOMPOSITION TECHNIQUE

The wavelet transform can decompose the signal, providing a useful description of the signal in both time and frequency or scale. The wavelet multiresolution analysis uses the discrete wavelet transform and its inverse transform to convert a signal into the sum of a number of wavelet components at different scales, which is an orthogonal and linear decomposition technique. The size of the wavelet basis function used in the wavelet transform is automatically adjusted, i.e., "automatic zooming," as frequency varies. The orthogonality and automatic zooming effect allow highly efficient algorithms to be devised for decomposing a signal into its wavelet components at different scales. Either discrete wavelet transform or wavelet multiresolution analysis has been used to analyze various flow phenomena [7,9–11]. Recently, Rinoshika and Zhou [12] applied the orthogonal wavelet multiresolution technique to the analysis of a turbulent near-wake. The same technique is used in this work and briefly described below.

A. Wavelet multiresolution analysis

For a one-dimensional function $v(x)$ and orthogonal wavelet basis $\Psi_{m,n}(x)$, the discrete wavelet transform is defined by

$$Dv_{m,n} = \sum_i v(x^i)\Psi_{m,n}(x^i). \tag{1}$$

In Eq. (1), $Dv_{m,n}$ represents a discrete wavelet transform coefficient, where m and n are the wavelet level and the location, respectively.

As an orthogonal transform, the discrete wavelet transform has the inverse transform and the original function can be reconstructed from the inversion of $Dv_{m,n}$, viz.,

$$v(x) = \sum_m \sum_n Dv_{m,n}\Psi_{m,n}(x). \tag{2}$$

The wavelet multiresolution analysis uses the discrete wavelet transform, Eq. (2), to decompose a function into the sum of a number of wavelet components at different central frequencies, viz.,

$$v = \sum_{i=1}^{N} v_i, \tag{3}$$

where v_i represents the wavelet component at the ith level, given by

$$v_i = \sum_n Dv_{i,n}\Psi_{i,n}(x). \tag{4}$$

The procedures of the wavelet multiresolution analysis may be summarized as follows.

(i) Wavelet coefficients are calculated from Eq. (1).

(ii) Apply the inverse wavelet transform, i.e., Eq. (4), to the wavelet coefficients of each level to yield wavelet components v_i.

The sum of all frequency components is a reconstruction of the original function. Therefore, the wavelet multiresolution analysis may decompose the function in both Fourier and physical spaces. In this study, the Daubechies family

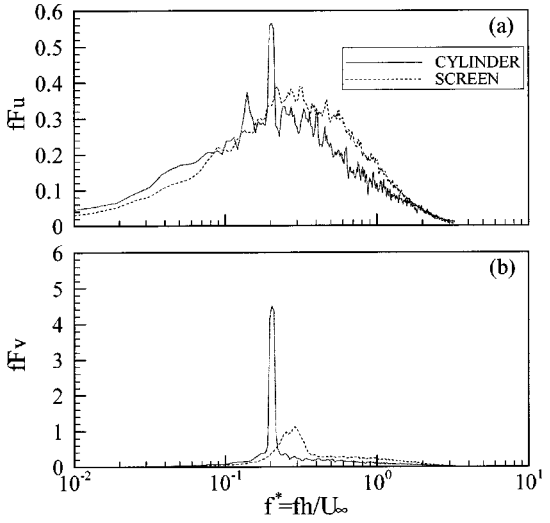

FIG. 1. Spectra of the measured u and ν signals at $y/h \approx 0.7$.

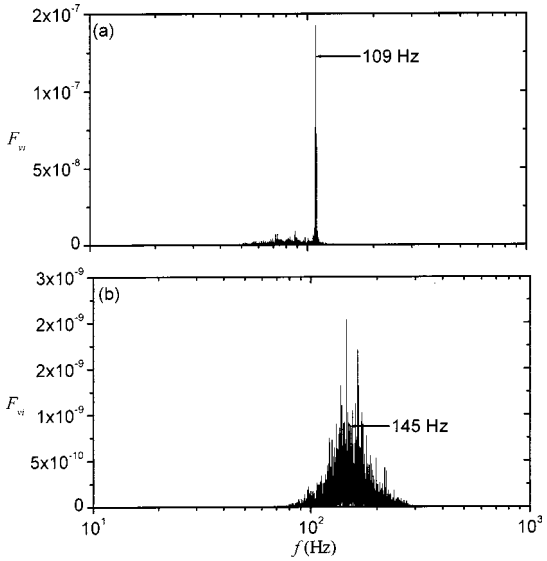

FIG. 2. Spectra of the wavelet components of ν signals at $y/h \approx 0.7$. (a) Circular cylinder: wavelet level 9; (b) screen: wavelet level 10.

with an index of $N=20$ is selected for the orthogonal wavelet basis.

B. Wavelet decomposition of velocity

An instantaneous velocity component V_k can be written as the sum of a time-averaging component $\overline{V_k}$ and a fluctuation component ν_k, viz.,

$$V_k = \overline{V_k} + \nu_k, \tag{5}$$

where the subscript $k=1$, 2, and 3 represents the velocity components in the x, y, and z directions, respectively. Using the wavelet multiresolution technique, ν_k is decomposed into a number of orthogonal wavelet components based on the central frequencies/wavelet levels, which are directly linked to the turbulent structure scales. Each wavelet component represents the turbulent structures of a certain range of frequencies (i.e., a nonzero frequency bandwidth) so that the information of any scales contained in the original data will not be lost because of a limited number of wavelet levels. In line with Eq. (3), the instantaneous wavelet component of velocity is given by

$$V_k = \overline{V_k} + \sum_{i=1}^{N} \nu_{k,i}, \tag{6}$$

where $\nu_{k,i}$ is the wavelet component of ν_k at the ith wavelet level.

C. Central frequencies and their bandwidth of wavelet components

A fundamental or dominant central frequency of turbulent structures has to be determined prior to the wavelet multiresolution analysis. This frequency is selected at the averaging frequency of Kàrmàn vortices in this study. The power spectra fF_u and fF_ν of the u and ν signals at $y/h \approx 0.7$, which is approximately on the vortex path, are shown in Fig. 1. The power spectral density functions F_u and F_ν are weighted by frequency f to indicate the energy distribution with f. There is a significant difference in spectra between the two wake generators. This is more evident in fF_ν. Both fF_u and fF_ν in the cylinder wake show a pronounced peak at the frequency $f_0^* = f_0 h/U_\infty \approx 0.2$, the well-known vortex shedding frequency

TABLE II. Central frequencies and bandwidths of wavelet components.

Circular cylinder			Screen		
Wavelet level	Central frequency (Hz)	Frequency bandwidth (Hz)	Wavelet level	Central frequency (Hz)	Frequency bandwidth (Hz)
8	55 ($f_0/2$)	25–65	9	73 ($f_0/2$)	45–130
9	109 (f_0)	45–135	10	145 (f_0)	70–280
10	218 ($2f_0$)	80–270	11	290 ($2f_0$)	150–550
11	436 ($4f_0$)	160–500	12	580 ($4f_0$)	300–1150
12	872 ($8f_0$)	300–1100	13	1160 ($8f_0$)	600–1750

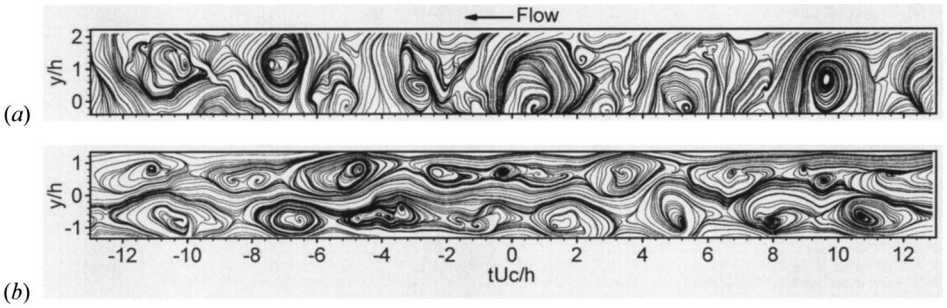

FIG. 3. Measured instantaneous sectional streamlines: (a) circular cylinder; (b) screen. The origin of time is arbitrary.

or Strouhal number in a circular cylinder wake. It is pertinent to comment that in the screen wake F_u does not show any pronounced peak, but F_ν does at the frequency $f_0^* \approx 0.27$, indicating the occurrence of large-scale vortical structures. Therefore, the averaging frequency, f_0 (=109 Hz for the circular cylinder and 145 Hz for screen), of large-scale vortical structures is specified as the fundamental central frequency.

In order to determine the frequency characteristics of each wavelet component, the ν signal at $y/h \approx 0.7$ is analyzed using the wavelet multiresolution technique, which yields 13 wavelet levels or components. The spectrum obtained from the Fourier analysis of each wavelet component displays a peak, which represents the central frequency, and spreads over a range of frequencies. Figure 2 displays the spectra of wavelet level 9 for cylinder and wavelet level 10 for screen, whose central frequency, identified with the most pronounced peak, corresponds to the fundamental central frequency f_0. Subsequently, the central frequencies of wavelet level 8, 10, 11, and 12 for cylinder and 9, 11, 12 and 13 for screen correspond to $\frac{1}{2}f_0$ $2f_0$, $4f_0$, and $8f_0$, respectively. The wavelet components from $\frac{1}{2}f_0$ to $8f_0$ cover the range of frequencies that are of major concern in the present investigation. These central frequencies and their bandwidths are given in Table II. Evidently, these central frequencies correspond to the scales of turbulent structures, and comparison between the turbulence structures of the comparable scale between the two wakes may be reduced to that between the wavelet components of the same multiple of f_0.

IV. TURBULENT STRUCTURES OF VARIOUS SCALES

In order to examine the turbulent structures of various scales, sectional streamlines [14], referred to as streamlines hereafter for simplicity, were constructed from the velocity vectors, i.e., (U_i, V_i), of each wavelet component as well as from measured velocity vectors. The streamlines are viewed in a reference frame translating at the convection velocity of the large-scale structures, which is $U_c = 0.87U_\infty$ [15] and $0.95U_\infty$ [16] for the cylinder and the screen wake, respectively.

Figure 3 shows the measured instantaneous streamlines in the (x,y) plane. The same scales have been used in the x and y directions to avoid the distortion of flow patterns. The vortical structures exhibit a striking difference in geometrical shape, size, and spacing between the two wake generators. However, only the large-scale structures are evident. It would be difficult to study the behaviors of the structures other than the large-scale ones for either flow.

Figures 4–6 present streamlines of different scales in the (x,y) plane for the circular cylinder and screen wakes, calculated from the wavelet components of velocity at the central frequencies of f_0, $2f_0$, $4f_0$, and $8f_0$. Streamlines were not constructed for the wavelet components of central frequencies higher than $4f_0$ since the convection velocity U_c of large-scale structures, at which the reference frame of streamlines translates, may not be appropriate for relatively small-scale structures. Perry and Chong [14] proposed to use the theory of critical points to describe eddy motions and flow patterns. Zhou and Antonia [13] successfully applied this theory to studying the topological details and three-dimensional aspects of a turbulent wake. Critical points, in particular foci and saddle points, represent the major topological characteristics of the flow. In general, the foci of the streamlines in Figs. 4–6 coincide with the local peaks of spanwise vorticity (not shown), calculated based on the velocity data, suggesting that information on the flow structure can be obtained by examining streamlines.

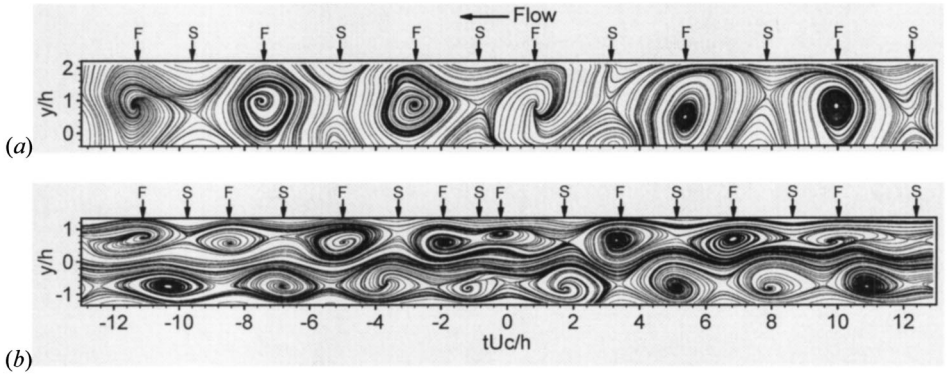

FIG. 4. Sectional streamlines of the wavelet component at f_0: (a) circular cylinder; (b) screen. The origin of time is arbitrary.

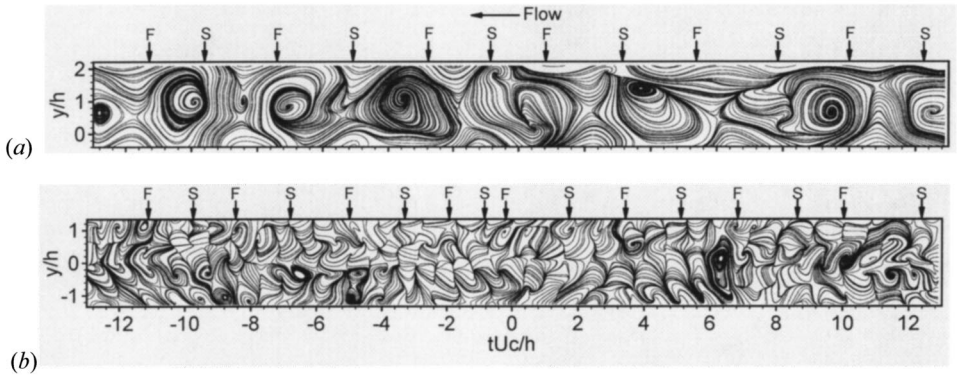

FIG. 5. Sectional streamlines of the wavelet component at $2f_0$: (a) circular cylinder; (b) screen. The origin of time is arbitrary.

Figure 4(a) displays six vortical structures in the cylinder wake, corresponding quite well to the large-scale structures in Fig. 3(a). The foci and saddle points, as denoted by *F* and *S* in Fig. 4, respectively, coincide approximately with those in Fig. 3 associated with large-scale structures. But the structures in Fig. 4 appear better organized and exhibit a much stronger periodicity. The observation indicates a correspondence between the wavelet component of the central frequency f_0 and the large-scale vortical structures. Figure 4(b) exhibits eight pairs of vortices in the screen wake. These structures correspond quite well to the large-scale structures in Fig. 3(b), and their occurrence is rather periodic. They are apparently the uppermost and energy-containing structures. There is a great difference in vortical structures between the two wakes. The structures in the circular cylinder wake are more energetic than those in the screen wake; their size is significantly larger. Furthermore, the vortices in the screen wake appear more elliptical in shape. These differences reflect basic differences in the vortex formation mechanisms. The vortices in the circular cylinder wake originate from the boundary layer separation from the cylinder, while those in the screen wake are likely to arise from the shear layer instability in the developing wake [16]. Correspondingly, the former, when advected downstream, are characterized by a decaying strength; the latter may have an increasing strength in the near-wake [17].

As the central frequency increases to $2f_0$, as shown in Fig. 5, we see the structures of a higher frequency but smaller size than those in Fig. 4. Some of them are apparently associated with the large-scale vortices of f_0 (Fig. 4), for example at $tU_c/h \approx -7$ and 9.6 in the circular cylinder wake and at $tU_c/h \approx -0.2$ and 3.6 in the screen wake. Others correspond to the saddle region between the large-scale vortices, such as at $tU_c/h \approx -0.8$ and 3.8 in the circular cylinder wake and at $tU_c/h \approx 1.8$ and 11.6 in the screen wake. The latter structures are consistent with the occurrence of longitudinal or rib structures, which occur between successive spanwise structures [13,18,19].

The size of the vortical structure in the circular cylinder wake appears larger than that in the screen wake. This is possibly related to the difference in the vortex generation mechanism between the two wakes. In the cylinder wake, vortices shed from the cylinder are energetic and large in size [Fig. 4(a)]. Furthermore, they have a relatively small spacing, both laterally and longitudinally. Their interactions are expected to be vigorous, producing a strong straining motion and vortex stretching, which is responsible for the longitudinal structures, in the saddle region between spanwise structures. In the screen wake, however, vortices originated from the shear layer instability in the developing wake are relatively weak and small in size [Fig. 4(b)], their spacing being large laterally and longitudinally. Consequently, the straining motion and vortex stretching between large-scale structures are weak, thus resulting in relatively weak intermediate-scale structures.

Once the central frequency reaches $4f_0$ (Fig. 6), the structures of smaller scale appear all over the flow. The structures in the circular cylinder wake appear considerably larger than those in the screen wake.

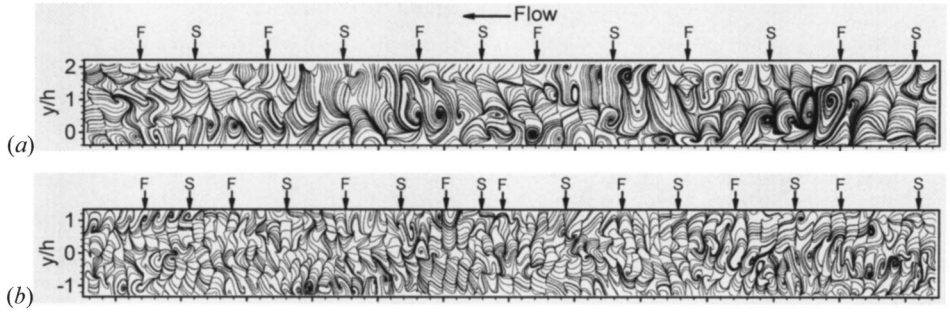

FIG. 6. Sectional streamlines of the wavelet component at $4f_0$: (a) circular cylinder; (b) screen. The origin of time is arbitrary.

V. CONTRIBUTIONS TO THE REYNOLDS STRESSES AND VELOCITY CORRELATION FROM DIFFERENT WAVELET COMPONENTS

The time-averaged product of the wavelet components β_i and γ_i, each representing u_i, ν_i, may be calculated by

$$\overline{\beta_i \gamma_i} = \frac{1}{n}\sum_{j=1}^{n} \beta_i \gamma_i, \tag{7}$$

where n is the total number of data points. The calculated $\overline{\beta_i \gamma_i}$ is normalized by the maximum value, $(\overline{\beta\gamma})_{\max}$, of the measured $\overline{\beta\gamma}$ so as to indicate the contribution from each wavelet component or central frequency to the Reynolds stresses.

A. Reynolds stresses

Figure 7 presents the lateral distributions of $\overline{\beta_i \gamma_i}$, as compared with the measured values for the circular cylinder and screen wakes. The wavelet components at a central frequency lower than $\frac{1}{2}f_0$ do not seem to be physically important, and those at a frequency higher than $8f_0$ only contribute about 1% or even smaller to Reynolds stresses. These components are therefore not included. The negative $\overline{u_i \nu_i}/(\overline{u\nu})_{\max}$ near $y/h=0$ and at relatively high central frequencies has been removed in Fig. 7(c) to allow the log-scale presentation. The $(\overline{\beta\gamma})_{\max}$ values (see Table III) show a discernible difference between the circular cylinder and the screen wakes, in particular for $(\overline{u^2})_{\max}$ and $(\overline{\nu^2})_{\max}$. The observation conforms to the results of Zhou and Antonia [5], suggesting the effect of different generators.

The total contribution from the components of $\frac{1}{2}f_0$, f_0, $2f_0$, $4f_0$, and $8f_0$ accounts for about 80% of $\overline{u^2}$, 95% of $\overline{\nu^2}$, and 85% of $\overline{u\nu}$; the five components are reasonably representative of the flow in terms of $\overline{\nu^2}$ and $\overline{u\nu}$, but not so in $\overline{u^2}$. It has been verified that errors caused by neglecting the frequencies higher than $8f_0$ are negligible. The u spectrum [Fig. 1(a)] exhibits significant energies at frequencies lower than $\frac{1}{2}f_0$, that is, the deficit between $\overline{u^2}$ and the contribution from the five components is mostly due to excluding those components of the central frequencies lower than $\frac{1}{2}f_0$.

The distributions of $\overline{\beta_i \gamma_i}/(\overline{\beta\gamma})_{\max}$ are similar to that of the measured data for both circular cylinder and screen, varying greatly with the central frequency. For $y/h>1.2$, $\overline{\beta_i \gamma_i}/(\overline{\beta\gamma})_{\max}$ of the screen wake is smaller than that of the circular cylinder wake and tends to fall off quickly. The wavelet component of f_0 represents the large-scale vortical structures, the corresponding $\overline{\beta_i \gamma_i}/(\overline{\beta\gamma})_{\max}$ in the screen wake being larger than that in the circular cylinder wake for $y/h<1.0$ (not so evident in Fig. 7 because of the use of a log scale). The observation suggests that the coherent contribution from the large-scale vortical structures to the Reynolds stresses is larger in the screen near-wake than in the solid body near-wake. The result reconfirms the conception that the large-scale vortical structures contribute to the effect of initial conditions. Furthermore, the difference between the wakes is appreciable down to the wavelet components of $4f_0$, suggesting that the intermediate-scale structures also play a role in the persistence of the initial conditions. In general, $\overline{\beta_i \gamma_i}/(\overline{\beta\gamma})_{\max}$ decreases as the central frequency increases, being consistent with the perception that the lower-frequency eddies are energy-containing. For the central frequency greater than $4f_0$, $\overline{\beta_i \gamma_i}/(\overline{\beta\gamma})_{\max}$ tends to drop quickly, approaching zero.

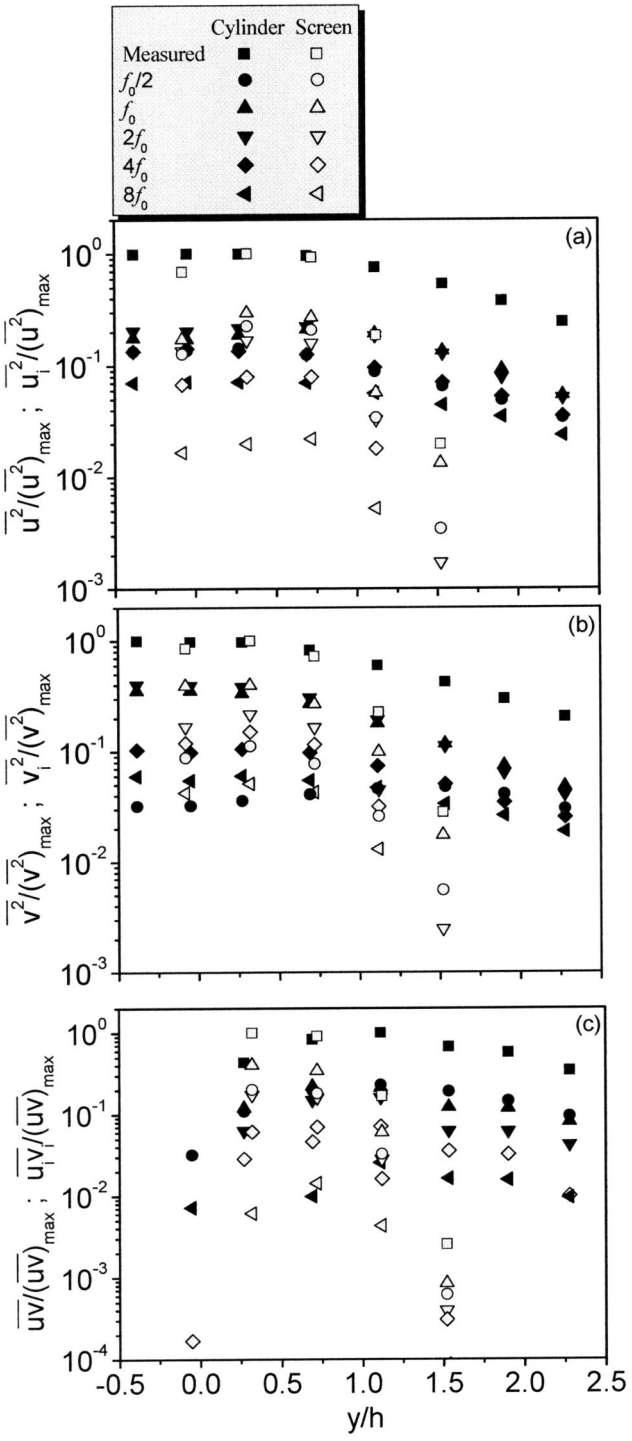

FIG. 7. Velocity variance and shear stress of the measured and the wavelet components at various central frequencies: (a) $\overline{u^2}/(\overline{u^2})_{\max}$ and $\overline{u_i^2}/(\overline{u^2})_{\max}$; (b) $\overline{\nu^2}/(\overline{\nu^2})_{\max}$ and $\overline{\nu_i^2}/(\overline{\nu^2})_{\max}$; (c) $\overline{u\nu}/(\overline{u\nu})_{\max}$ and $u_i\nu_i/(\overline{u\nu})_{\max}$.

TABLE III. Maximum values of $\overline{u^2}/U_\infty^2$, $\overline{v^2}/U_\infty^2$, and $\overline{uv}/U_\infty^2$.

	$\overline{u^2}/U_\infty^2$	$\overline{v^2}/U_\infty^2$	$\overline{uv}/U_\infty^2$
Circular cylinder	1.42×10^{-2}	2.53×10^{-2}	-2.27×10^{-3}
Screen	4.9×10^{-3}	3.92×10^{-3}	-2.18×10^{-3}

In the case of the circular cylinder wake, $\overline{u_i^2}/(\overline{u^2})_{\max}$ and $\overline{v_i^2}/(\overline{v^2})_{\max}$ of $2f_0$ are very close to that of f_0, implying that energies associated with the two central frequencies are quite comparable and the contribution from the intermediate-scale structures is significant to the total Reynolds stresses. As a matter of fact, the former even exceeds, though slightly, the latter near the centerline. This is because the lateral spacing between the two rows of vortices is small in the near-wake and thus the most prominent peak in the u spectrum (not shown) occurs at the second harmonic ($2f_0$) of the vortex shedding frequency near the center line. Furthermore, the wavelet components at f_0 and $2f_0$ are most energy-containing, accounting for almost 43%, 74%, and 40% of $(\overline{u^2})_{\max}$, $(\overline{v^2})_{\max}$, and $(\overline{uv})_{\max}$, respectively. When the central frequency increases from $2f_0$ to $4f_0$, the value of the wavelet component appears falling off rather rapidly, up to about 11% of the measured value for $\overline{v_i^2}/(\overline{v^2})_{\max}$.

For the screen wake, $\overline{\beta_i\gamma_i}/(\overline{\beta\gamma})_{\max}$ of f_0 remains everywhere largest and responsible for almost 40%, 29%, and 40% of $(\overline{u^2})_{\max}$, $(\overline{v^2})_{\max}$, and $(\overline{uv})_{\max}$, respectively, suggesting that the greatest contribution to the total Reynolds stresses comes from the large-scale structure in the screen wake. As the central frequency increases from f_0 to $2f_0$, the decrease is rather rapid, up to 17–22% of the measured $(\overline{\beta\gamma})_{\max}$, compared with the cylinder wake.

The above observation indicates that the most significant contribution to the Reynolds stresses comes from the turbulence structures of f_0 and $2f_0$ in the cylinder wake. However, in the screen wake, the contribution to Reynolds stresses comes primarily from the turbulence structures of f_0; the role played by those of $2f_0$ appears to be less significant than that in the cylinder wake. This is a significant difference between the two wakes.

It is pertinent to comment that in the cylinder wake, $\overline{v_i^2}/(\overline{v^2})_{\max}$ (74%) corresponding to f_0 and $2f_0$ overwhelms $\overline{u_i^2}/(\overline{u^2})_{\max}$ (43%), which is similar to the behavior of the coherent contribution from the large-scale structures in solid bluff-body wakes [13]. In contrast, $\overline{u_i^2}/(\overline{u^2})_{\max}$ (40%) at f_0 exceeds $\overline{v_i^2}/(\overline{v^2})_{\max}$ (29%) in the screen wake, resembling the behavior of the coherent contribution from the large-scale structures in a turbulent far-wake [16]. The different behavior between the large-scale structures in the two wakes is consistent with the fact that their vortex generation mechanisms are not the same.

B. Correlation coefficient of various scales

It is well known that the large-scale structures in a cylinder near-wake originate from a mechanism different from that in a screen near-wake. Therefore, these structures behave very differently between the two wakes. They may further influence the behaviors of intermediate- or even small-scale structures, as shown earlier in this paper. The two-dimensionality of the wavelet components is therefore examined for the two wakes.

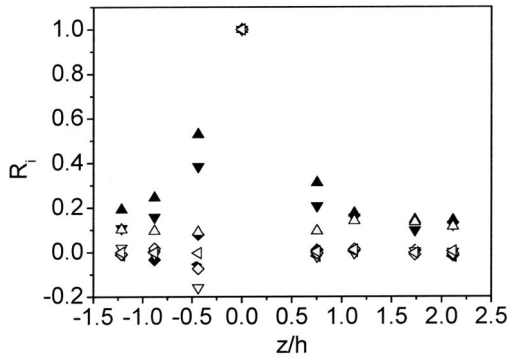

FIG. 8. Spanwise variation of the correlation coefficient, $R_i=\overline{u_{z0i}u_i}/[(\overline{u_{z0i}^2u_i^2})^{1/2}]$, of the wavelet components at various central frequencies. The symbols are as in Fig. 7.

To estimate the spanwise extent of the turbulent structures of different scales, the correlation coefficient of the wavelet component [12], R_i, between u_i from X wires in the (x,z) plane and u_{z0i} from the X wire in the (x,y) plane that is closest to the (x,z) plane, is defined as

$$R_i = \frac{\overline{u_{z0i}u_i}}{(\overline{u_{z0i}^2u_i^2})^{1/2}}. \tag{8}$$

The spanwise variation of R_i is shown in Fig. 8. Evidently, R_i decreases as the central frequency increases. This is reasonable since the larger-scale structures are more "two-dimensional" than those smaller-scale structures. The correlation coefficients corresponding to f_0 up to $2f_0$ in the cylinder wake are considerably larger than that in the screen wake, implying that the large- and intermediate-scale structures are much more two-dimensional than those in the screen wake. This is expected. The large-scale spanwise structures are shed from the cylinder in the form of "rolls," whereas the intermediate-scale structures as represented by the wavelet component of $2f_0$ possibly result from vigorous interactions between the large-scale spanwise structures and may naturally inherit two-dimensionality from those of f_0. On the other hand, vortical structures in the screen wake originate from the shear layer instability of the developing wake, more likely to exhibit smaller length scales, especially in the spanwise direction, than those shed from a cylinder.

VI. CONCLUSIONS

The near-wake generated by a screen and a circular cylinder, respectively, has been investigated with a view to provide information on the effect of initial conditions on turbulence structures of various scales by using the wavelet multiresolution technique. The instantaneous sectional streamlines of various scales have been examined. The contributions to the Reynolds stresses and velocity correlation from the motions of various scales have also been quantified. The following conclusions can be drawn.

(i) The behaviors of the wavelet component of f_0 are consistent with those of the conditionally averaged large-scale structures for both wake generators [5]. These large-scale structures, along with those of intermediate scales, exhibit a strong dependence upon the initial conditions.

(ii) The contributions to the Reynolds stresses are comparable from the turbulent structures of f_0 and $2f_0$ in the cylinder wake, their combined contribution accounting for 43%, 74%, and 40% to $(\overline{uv})_{\max}$, $(\overline{u^2})_{\max}$, and $(\overline{v^2})_{\max}$, respectively. In the screen wake, however, the structures of f_0 make a contribution considerably higher than other wavelet components, responsible for almost 40%, 29%, and 40% to $(\overline{uv})_{\max}$, $(\overline{u^2})_{\max}$, and $(\overline{v^2})_{\max}$, respectively.

(iii) The large- and intermediate-scale structures in the cylinder wake appear much more two-dimensional than those in the screen wake.

ACKNOWLEDGMENTS

The experiments were conducted at Professor R. A. Antonia's laboratory at The University of Newcastle with the financial support from Australian Research Council. A.R. wishes to acknowledge support given to him by a Grant-in-Aid for Scientific Research (C) (No. 13650189) from the Japanese Society for the Promotion of Science. Y.Z. wishes to acknowledge support by the Research Grants Council of the Government of the HKSAR through Grant No. B-Q862.

[1] K. R. Sreenivasan, AIAA J. **19**, 1365 (1981).
[2] I. Wygnanski, F. Champagne, and B. Marasli, J. Fluid Mech. **168**, 31 (1986).
[3] P. R. Louchez, J. G. Kawall, and J. F. Keffer, *Lecture Notes in Physics* (Springer, New York, 1987), p. 98.
[4] M. Matsumura, Z. Huang, J. G. Kawall, and J. F. Keffer, in *Proceedings of the 8th Symposium on Turbulent Shear Flows*, No. 28-2-1 (1991).
[5] Y. Zhou and R. A. Antonia, AIAA J. **32**, 1207 (1994).
[6] M. Farge, Annu. Rev. Fluid Mech. **24**, 395 (1992).
[7] C. Meneveau, J. Fluid Mech. **232**, 469 (1991).
[8] H. Li, ASME J. Fluids Eng. **120**, 778 (1998).
[9] M. Farge, K. Schneider, and N. Kevlahan, Phys. Fluids **11**, 2187 (1999).
[10] H. Mouri, H. Kubotani, T. Fujitani, H. Niino, and M. Takaoka, J. Fluid Mech. **389**, 229 (1999).
[11] H. Li, H. Hu, T. Kobayashi, T. Saga, and N. Taniguchi, AIAA J. **40**, 1037 (2002).
[12] A. Rinoshika (H. Li) and Y. Zhou, J. Fluid Mech. **524**, 229 (2005).
[13] Y. Zhou and R. A. Antonia, J. Fluid Mech. **275**, 59 (1994).
[14] A. E. Perry and M. S. Chong, Annu. Rev. Fluid Mech. **19**, 125 (1987).
[15] Y. Zhou and R. A. Antonia, Exp. Fluids **13**, 63 (1992).
[16] Y. Zhou and R. A. Antonia, Exp. Fluids **19**, 112 (1995).
[17] H. J. Zhang and Y. Zhou, Phys. Fluids **13**, 3675 (2001).
[18] A. K. M. F. Hussain and M. Hayakawa, J. Fluid Mech. **180**, 193 (1987).
[19] H. J. Zhang, Y. Zhou, and R. A. Antonia, Phys. Fluids **12**, 2954 (2000).